PIER

Miniaturized Dual-Polarized, High-Gain, and Wideband Dielectric Resonator Antenna for Low Band Massive MIMO Applications

Ahmed El Yousfi[1,*], Kerlos Atia Abdalmalak[1,2], Abdenasser Lamkaddem[1], Alejandro Murrillo Barrera[3], Bruno Biscontini[3], and Daniel Segovia Vargas[1]

[1]*Signal Theory and Communication Department, the University Carlos III of Madrid, Madrid 28911, Spain*
[2]*Electrical Engineering Department, Aswan University, Aswan 81542, Egypt*
[3]*German Research Center, Huawei Technologies Duesseldorf GmbH, Munich 80992, Germany*

ABSTRACT: A new dual-polarized compact crossed-notched dielectric resonator antenna (DRA) with high-gain and wideband performance is proposed for low-band massive multiple-input multiple-output (MIMO) applications at the 700 MHz band of 5G new radio (5G NR) technology. The DRA element consists of three dielectric layers with relatively high relative permittivity constants ($\epsilon_{r1} = 15$ for the bottom and top layers and $\epsilon_{r2} = 23$ for the middle one) for a compact antenna. Characteristic mode analysis (CMA) of a rectangular DRA reveals that two pairs of degenerate modes, namely M2/M3 and M4/M5, resonating at 0.4 and 0.6 GHz respectively can be used to achieve dual polarizations with a proper feeding strategy. By jointly reshaping the conventional DRA along with adding a notch into the middle dielectric layer, the two pairs of degenerate modes are merged to produce a broad bandwidth with a compact size of $0.2\lambda_{\max} \times 0.2\lambda_{\max}$ ($\lambda_{\max}$ being the wavelength at low-frequency point). The measured results show an impedance bandwidth of 13.15% (710 MHz–810 MHz) and an isolation of less than -17 dB. Furthermore, the antenna exhibits a good radiation pattern over the working band with a high gain of 7 dB. Finally, the proposed element is tested in a massive MIMO system of 3×4. The results exhibit a wideband of 17.7% and high isolation of more than 12 dB along with a stable gain of 5 dBi within the operating band.

1. INTRODUCTION

Nowadays the demand for high capacity and large through-put rate in wireless communications is substantially rising. For this, 5G massive MIMO technology is a good solution that has been widely investigated in recent years. However, most work has been undertaken on high-frequency bands (frequencies above 1.7 GHz). So, the possibility of increasing the MIMO order in the low-frequency bands (frequencies below 1 GHz) is very promising and challenging. On the one hand, the application of massive MIMO at the lowest 5G band will enable a wider coverage, essential for covering a massive number of IoT devices. On the other hand, designing a small antenna at a low frequency (700 MHz) band is very hard because of the inherent large size in a limited space. Therefore, the need for compact and miniaturized broadband antennas along with high gain performance is in high demand for massive MIMO applications. Finally, dual-polarization radiation is requested to increase channel capacity and reduce multipath effect because of polarization diversity.

In recent years, several wideband dual-polarized antennas based on conventional geometries have been developed for 5G base station applications such as dipoles [1, 2], patches [3–5], and slot antennas [6, 7]. However, most of the previous designs suffer from relatively large sizes and need larger band-

widths. Recently, DRAs have received much attention owing to their properties such as the elimination of conductors' ohmic losses and high gain. Mostly, DRAs are designed in substrates with high relative dielectric permittivity constant ϵ_r (usually larger than 7) which means that the DRAs are compact designs [8]. For more compactness, higher ϵ_r values are used. This is achieved at a price of both a severe degradation in the bandwidth due to the high-quality factor Q and low gain. This problem can be seen in [9], where a relative permittivity of 38 was used to miniaturize a dual-polarized and dual-band DRA down to $0.14\lambda_{\max} \times 0.14\lambda_{\max}$ but with a tiny 4% bandwidth and a gain as low as 2.8 dB. In [10], to overcome the previous drawbacks, a monolithic DRA with a high permittivity of 20.5 and two loaded metallic strips on the bottom of the cross dielectric, working as electric dipoles are used to excite a resonant pole and, at the same time, used to excite the mode TE_{11}^x of the DRA. These changes resulted in a 15% wideband with a stable high gain (8.5 dBi) over the frequency band. However, the size is somewhat large, $0.38\lambda_{\max} \times 0.38\lambda_{\max}$, which might not be suitable for massive MIMO base station applications.

Several other compact and/or broadband DRA designs have been proposed [11–15]. In [11], a metasurface loads the DRA along with a pair of shorting conducting walls. The metasurface generates an extra resonance while the shorting walls contribute to lowering the frequency. Although the bandwidth is increased up to 17% in compared with the unloaded DRA, the

* Corresponding author: Ahmed El Yousfi (aelyousf@ing.uc3m.es).
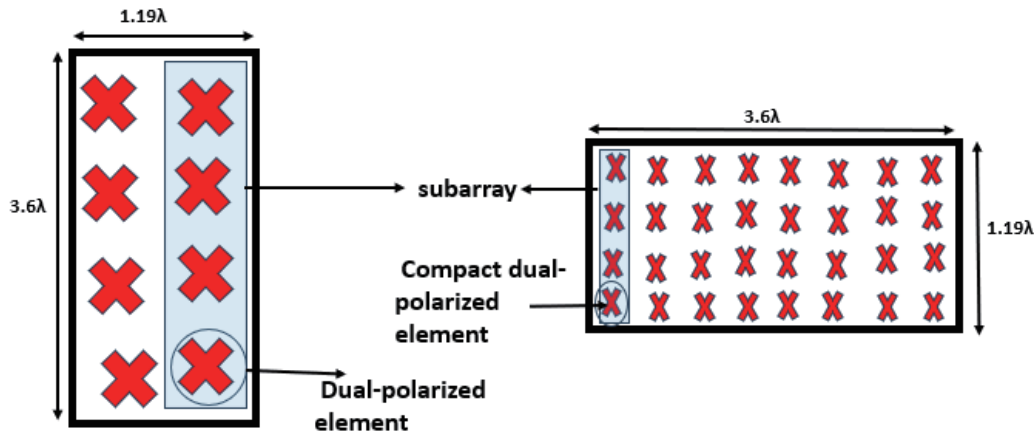
FIGURE 1. Current MIMO base station array (a) and new massive MIMO solution (b).

overall size is around half-wavelength $0.52\lambda_{\max} \times 0.52\lambda_{\max}$. A hybrid feeding circuit with conformal strips is used to excite a DRA, and as a result, a wide bandwidth of 21.9% and a compact size of $0.44\lambda_{\max} \times 0.44\lambda_{\max}$ are achieved [12]. Similarly, a new microstrip pair of coupled slots is used to feed and excite three modes of a DRA [13]. Consequently, a wide band of 20.3% is achieved, but at the expense of its large size of $0.63\lambda_{\max} \times 0.63\lambda_{\max}$. The use of artificial magnetic conductors has also been used to achieve a highly compact DRA design [14]. The miniaturization of 85% in size is obtained along with a bandwidth of 14.2%. A different idea is presented in [15] where a compact DRA design of size $0.4\lambda_{\max} \times 0.4\lambda_{\max}$ is achieved by using a conductive feeding assembly composed of a feeding network to excite a first DRA mode and a feeding probe to excite a second DRA mode. However, the resultant bandwidth is 9.5% which remains relatively low in comparison with the needs in wireless communications. Other works for 5G MIMO applications have been developed [16–23]. To the authors' knowledge, no compact, high-gain, and wideband DRA has been reported in the literature for massive MIMO 5G applications in the low-frequency band.

This work departs from our initial study [24] which mainly aimed at addressing the challenge of achieving massive MIMO in the 700 MHz band. This will need, at the same time, miniaturization of the radiating element while keeping good radiation performance such as high gain and wideband. Consequently, more transceiver (TRX) columns can be included without significantly increasing the total size of the array antenna. The increase of TRX columns would require either changing the chassis of the base transceiver station (BTS) antenna, which is not possible or reducing the size of the radiating element. The current MIMO base stations (See Fig. 1(a)) consist of vertically arranging the subarrays (namely 2×4 or 2×5) in a size of $1.19\lambda \times 3.6\lambda$ [25]. The solution that we propose consists of a new massive MIMO structure that reduces the size of the radiating element and horizontally places the whole system. We note that this selection is made after testing two massive MIMO systems placed initially vertically and later horizontally in terms of cell throughput which revealed that the latter one outperforms the vertical option. In this way, a much larger number

of subarrays will be supported by the current configuration, as seen in Fig. 1(b). Therefore, for miniaturization purposes, we use the high permittivity constant technique to design a compact multi-layer crossed-notched dielectric resonator antenna of size $0.2\lambda_{\max} \times 0.2\lambda_{\max}$. Although this technique results in narrow bandwidth [26], adding a notch into the middle layer of the DRA allows us to achieve a wide bandwidth of 18.2%. The rest of the paper is organized in the following way: Section 2 discusses the design of the single radiating element and its working principle based on characteristic mode analysis (CMA) and dielectric waveguide model (DWM). The simulated results and discussions including a unit cell antenna that is examined in a massive MIMO scenario are presented in Section 3. Fabrication and measurements are presented in Section 4. Finally, a conclusion is given in Section 5.

2. PROPOSED COMPACT BROADBAND AND DUAL-POLARIZED DIELECTRIC RESONATOR ANTENNA

2.1. Proposed Antenna Design

The proposed crossed-notched dielectric resonator antenna is shown in Fig. 2. It is composed of three dielectric blocks with different relative permittivities ($\epsilon_{r1} = 15$ with a loss tangent of 0.001 for the bottom and top blocks and $\epsilon_{r1} = 23$ with a loss tangent of 0.0037 for the middle one), and a ground plane. The first block is an inverted crossed horn with a bottom size of $0.13\lambda_{\max} \times 0.13\lambda_{\max}$ and an upper one of $0.2\lambda_{\max} \times 0.2\lambda_{\max}$, whereas the second and third blocks are crossed-hexagonal with dimensions of $0.2\lambda_{\max} \times 0.2\lambda_{\max}$. The height of the proposed DRA is 95 mm which is equal to $0.22\lambda_{\max}$ at 700 MHz and clearly fits the chassis of any modern BTS antenna. To get broadband performance a notch is inserted in the middle dielectric block together with changing the DRA geometry. Four-pin probes are used to feed the antenna and achieve $\pm 45°$ dual-polarization radiation as summarized in Table 1. It is worth noting that practically such a feeding method is achieved by inserting power dividers along with a phase shifter of $180°$ based on a meandered line for compactness purposes. Finally, in order to maintain the mechanical stability of the design, four screws
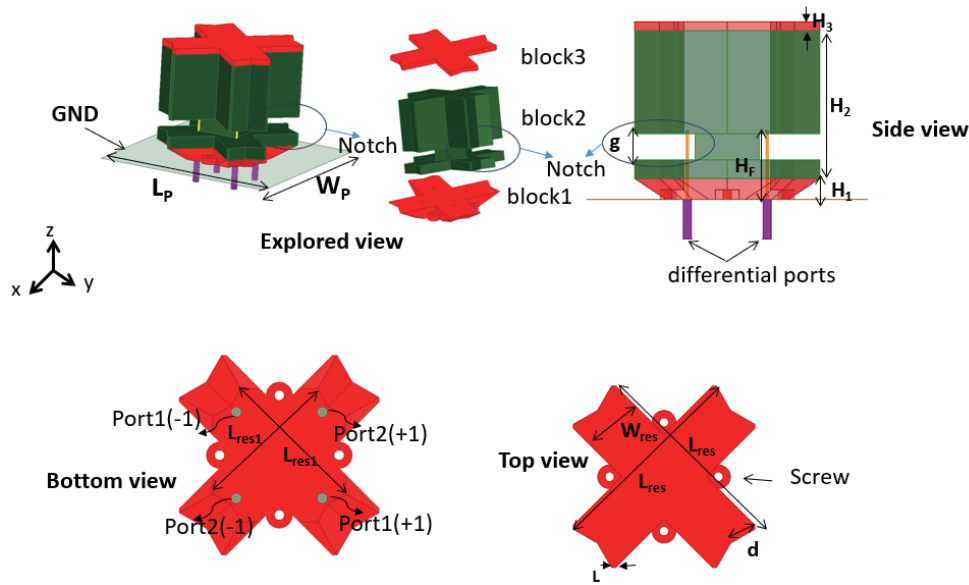
FIGURE 2. Proposed crossed-notched DRA.

TABLE 1. Feeding scheme of the dual-polarized DRA.

Ports	Port 1 $(A(\phi\cdot^{\circ})^{*},\ A(\phi\cdot^{\circ}))$	Port 2 $(A(\phi\cdot^{\circ}),\ A(\phi\cdot^{\circ}))$
$+45^{\circ}$	$(1(0), 1(180))$	$(0(0), 0(0))$
-45°	$(0(0), 0(0))$	$(1(0), 1(180))$

* $A(\phi\cdot^{\circ})$ represents the amplitude and the phase of the prot respectively.

TABLE 2. Optimized values of the proposed antenna.

Param.	W_{p}	L_{p}	g	W_{res}	L_{res}	H_{1}	H_{2}	H_{3}	L_{res1}	d	L
Value [mm]	150	150	14	32.6	110	11	5	79	73.4	15.3	2.2

have been added to the ground plane. The optimized values of the proposed antenna are given in Table 2.

2.2. Proposed Antenna Element and Working Principle

To understand the working principle of the proposed DRA, four design steps have been undertaken. The evolution steps of the proposed design are presented in Fig. 3 and analyzed using characteristic mode analysis (CMA) [8, 27]. Here, CMA is used as a guide tool to analyze the DRA so that proper modes can be excited efficiently to achieve ±45º dual polarizations with broadband performance. The convenient way to show the resonant frequency is modal significance (MS) which is defined as [8]:

$$MS = 1/|1 + j\lambda_{n}|. \quad (1)$$

where λ_{n} is the eigenvalue solved from the generalized eigenvalue equation. When $MS = 1$ indicates that the mode is resonant and can radiate, $MS = 0$ shows that the mode is non-resonant; therefore, the mode cannot radiate.

Firstly, the CMA is applied to Ant1. The simulations are done using FEKO software. The CMA setup consists of placing the DRA in the absence of the feeding source over an infinite ground plane which, according to image theory, will reduce the DRA height by half, thus the computation time will be decreased as well. The MS of the first 8 modes of Ant1 is displayed in Fig. 4. We note that other modes can exist. To get a clear vision of the modes, the corresponding modal magnetic field at the resonance frequency is shown in Fig. 5. On the one hand, with reference to Fig. 4, one can see that mode 1 resonates at 0.55 GHz with a wide bandwidth [8]; however, this mode will not be excited as its electric field component is in phase along the z-axis (not shown for brevity). On the other hand, it can be seen that modes 2/3 and 4/5 are degenerate modes. Modes 2/3 resonate at 0.434 GHz, and they are associated with $TE_{111}^{x,y}$ in the dielectric waveguide model (DWM) [28, 29] as clearly indicated in Figs. 5(b) and (c), whereas modes 4/5 resonate at 0.52 GHz which corresponds to $TE_{113}^{x,y}$ in DWM (shown in Figs. 5(d) and (e)). This will be extensively proven in what follows. We note that the origin of degeneracy is due to the
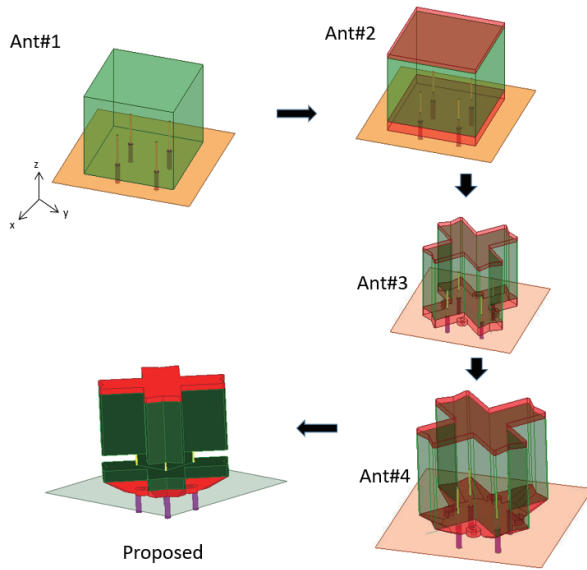
FIGURE 3. Evolution of the proposed crossed-notched DRA: Ant1 is the standard DRA, Ant2 is the multi-layer DRA, Ant3 is the cross-shaped DRA, and Ant4 is the cross-shaped DRA with horn-like base.
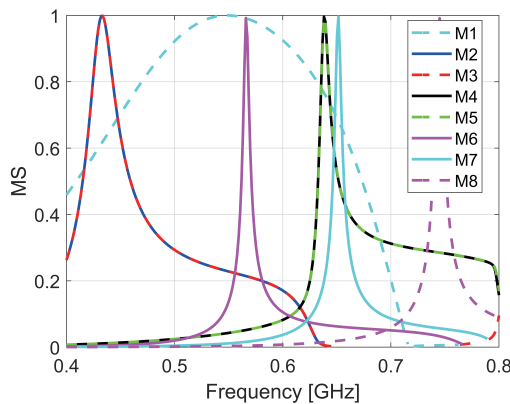
FIGURE 4. Modal significance of the reference Ant1 for the first eight modes.

equal length of DRA along the x- and y-axes. Mode 6 has a resonance at 0.56 GHz and is associated with TE_{111}^z. Finally, modes 7 and 8 resonate at 0.65 and 0.74 GHz, respectively. To examine which modes could be excited to obtain dual slant polarizations, the modal weighting coefficient (MWC) [8, 27, 30] is examined in Fig. 6. The MWC is obtained in the presence of differential feeding ports along the diagonal of the DRA (See Ant1 in Fig. 3) and is expressed as

$$MWC = \frac{<J_n, E^i>}{1 + j\lambda_n} = \frac{1}{1 + j\lambda_n} \iint_S J_n E^i \, ds \quad (2)$$

where E^i is the induced external electric field at the surface S. The MWC shows into which mode most of the power is coupled. Since the DRA is symmetric, only one differential feeding is excited (port 1 $(+1, -1)$). As expected, modes 2 and 4 are selectively excited as their MWC presents a maximum value around the frequency points of 0.4 and 0.6 GHz.

The same trace of MWC will be obtained in case port 2 is excited where modes 3 and 5 will be excited. This demonstrates that dual polarization radiation can be achieved at two distinct frequencies. Therefore, to achieve a wideband performance in the DRA, a reshaping technique of the DRA has to be done.

We note that modes $TE_{112n}^{x,y}$ $(n = 1, 2, 3, \ldots)$ are eliminated by the presence of the ground plane [31].

These results are very consistent with the dielectric waveguide model (DWM) [29] (See Table 3). According to this model, the resonance frequency can be calculated by the following equations [29]:

$$f_{mnl} = \frac{c}{2\pi\sqrt{\epsilon_r}} \sqrt{k_x^2 + k_y^2 + k_z^2}. \quad (3)$$

where

$$k_x = \frac{m\pi}{a}; \quad k_z = \frac{l\pi}{2d}; \quad k_y \tan\left(\frac{k_y b}{2}\right) = \sqrt{(\epsilon_r - 1)k_0^2 - k_y^2}. \quad (4)$$

$$k_x^2 + k_y^2 + k_z^2 = \epsilon_r k_0^2. \quad (5)$$

Secondly, it is expected that the characteristic mode analysis of Ant2 will be similar to that of Ant1 with the only difference being the use of two different relative permittivities (15 for the bottom and top layers and 23 for the middle one) which decreases the effective permittivity as shown in what follows. Hence, the CMA for this case is omitted.

Then, in an effort to bring the two pairs of modes closer to each other, thereby improving wideband performance, three main changes have been introduced into Ant2. First, the DRA's shape is modified to a cross-shape which constitutes the so-called Ant3. This has shifted the two pairs of degenerated modes to high frequencies as seen in Fig. 7. Compared to the MS of Ant1, it is observed that the modes are brought slightly together, but such difference is still not enough to achieve the broadband design. In the second modification, for more control of the two pairs of modes, the first dielectric block is modified to be horn-like (Ant4). From the MS of Ant4 in Fig. 8, it is seen that although the two pairs of degenerated modes are shifted to each other compared to Ant3, the broadband performance would be hard to attain. Therefore, another change must be added. We note that the MWC of these two antennas is not shown since the modes are not close enough to achieve wideband radiation.

Finally, adding a notch in the middle dielectric block allows additional degrees of freedom when being combined with the previously described geometrical modifications leading to the proposed design and enabling us to get broadband behavior. With respect to Fig. 9, it is seen that all modes are shifted towards the high-frequency band. One can also see that the bandwidth of the two pairs of degenerate modes is enhanced. More importantly, the two pairs are much more close to each other which may result in a wideband performance. Again, due to the symmetry of the design, only one differential port is excited as in Ant1 to examine MWC. Fig. 10 demonstrates that modes 2 and 4 are selectively excited. Therefore, broadband and dual polarization features can be obtained by careful tuning of remaining DRA parameters.
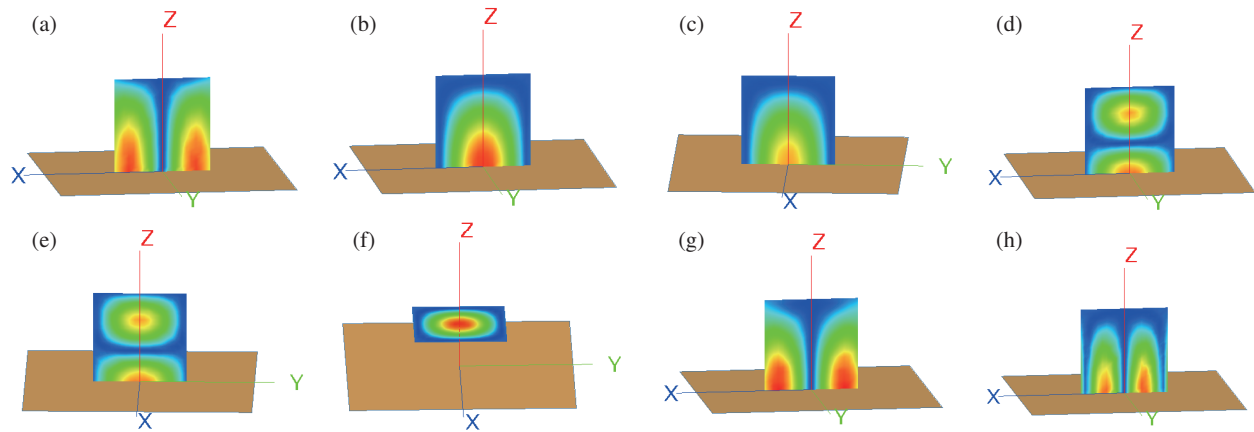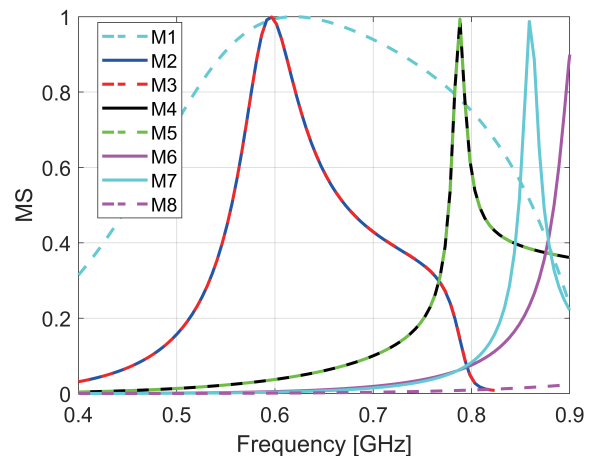
FIGURE 5. Modal dominant magnetic field components of the 8 modes. (a) H_y mode 1, (b) H_y mode 2, (c) H_x mode 3, (d) H_y mode 4, (e) H_x mode 5, (f) H_z mode 6, (g) H_y mode 7, (h) H_y mode 8.
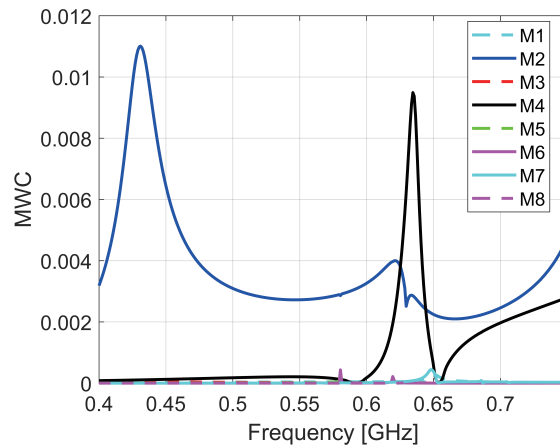
FIGURE 6. Modal weighting coefficient of the reference Ant1 with one differential port.
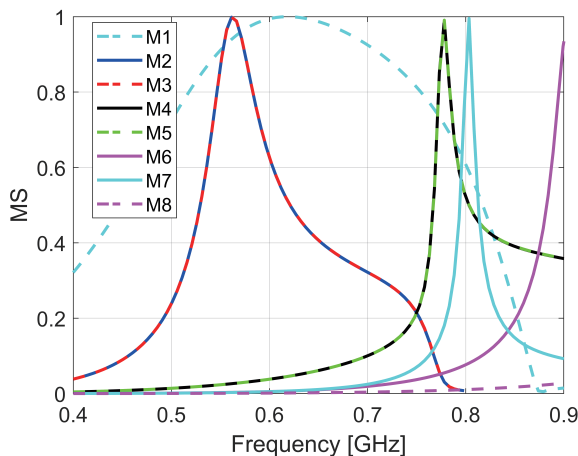
FIGURE 7. Modal significance of the Ant3 for the first eight modes.

FIGURE 8. Modal significance of the Ant4 for the first eight modes.

3. SIMULATION RESULTS AND DISCUSSIONS

3.1. Antenna Element

To verify the performances of the reference antennas shown in Fig. 3 with actual probes and finite ground plane, a full wave simulation is performed in HFSS. Fig. 11 shows the reflection coefficients of the evolution design steps. As it has been mentioned, to achieve dual slant polarizations ($\pm 45°$) the antenna is fed through two differential ports along the diagonal (Fig. 1): port 1 ($+1, -1$) and port 2 ($+1, -1$). The S-parameters of the
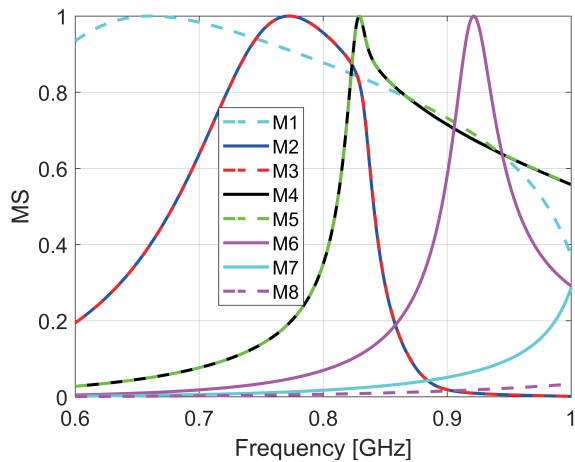
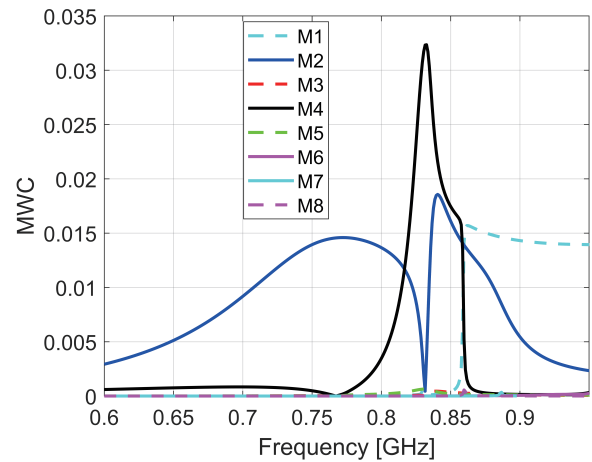**FIGURE 9**. Modal significance of the proposed DRA for the first eight modes.

FIGURE 10. Modal weighting coefficient of the proposed DRA with one differential port.

TABLE 3. Comparison between DWM, CMA, and full-wave simulation of resonances of Ant1.

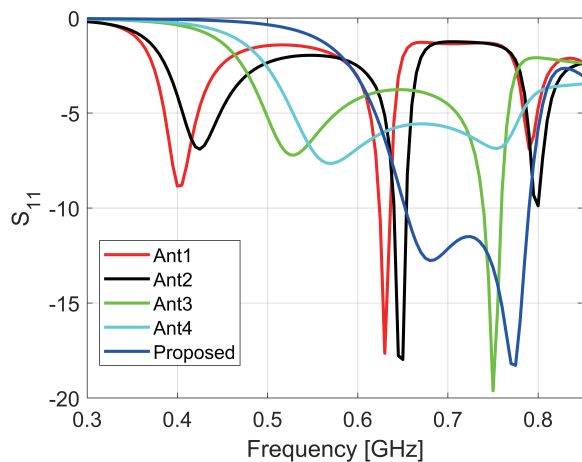| Modes	$f_{res}(DWM)[GHz]$	$f_{res}(CMA)[GHz]$	$f_{res}(HFSS)[GHz]$
$TE_{111}^{x,y}$	0.416	0.434 (M2/M3)	0.403
$TE_{113}^{x,y}$	0.635	0.643 (M4/M5)	0.630
HM	NA	0.75 (M8)	0.79

FIGURE 11. Reflection coefficient of the different reference antennas of Fig. 3.
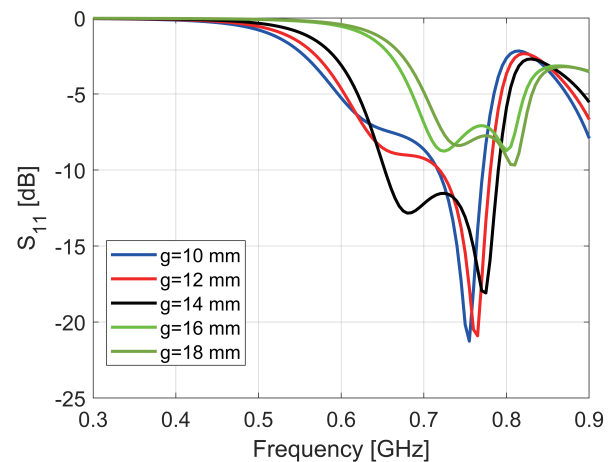

FIGURE 12. Effect of the variation of the gap height g on the reflection coefficient.

two differential ports are given as follows [32]:

$$S_{dd11} = (S_{11} + S_{22} - S_{12} - S_{21})/2. \quad (6)$$
$$S_{dd12} = (S_{13} + S_{24} - S_{14} - S_{23})/2. \quad (7)$$
$$S_{dd21} = (S_{31} + S_{42} - S_{41} - S_{32})/2. \quad (8)$$
$$S_{dd22} = (S_{33} + S_{44} - S_{34} - S_{43})/2. \quad (9)$$

We note that as the four designs are symmetric, only S_{dd11} and S_{dd12} are presented for the sake of brevity. As expected from CMA and DWM, the modes 2/3 (TE_{111}), 4/5 (TE_{113}), and 8 (which is considered hybrid mode (HM)) are excited, and

Ant1 covers a small bandwidth of 2% at 0.63 GHz because of the high permittivity. In the second step, a multi-layer rectangular DRA (the bottom and top layers have a permittivity of $\epsilon_{r1} = 15$, and the middle one of $\epsilon_{r2} = 23$) is presented and denoted as Ant2. This arrangement slightly shifted the resonances towards high frequencies in comparison with Ant1. This is due to the low effective dielectric constant of the whole DRA design which can be calculated according to [33] as follows:

$$\epsilon_{eff} = \frac{H_1 + H_2 + H_3}{H_1/\epsilon_{r1} + H_2/\epsilon_{r2} + H_3/\epsilon_{r1}}. \quad (10)$$
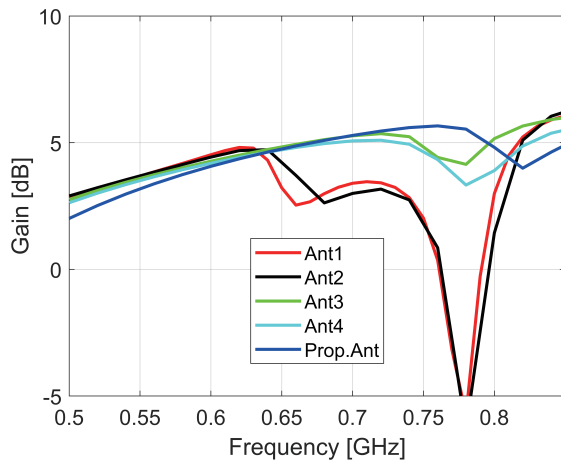
FIGURE 13. Gain comparison of different antenna designs steps of Fig. 3.

FIGURE 14. Simulated efficiency of the proposed antenna.

This results in an effective permittivity of 21.5 which is relatively low compared to Ant1. However, the bandwidth remains very small to cover the targeted band. It is also observed that the matching is generally improved [33]. We note that since the resonance frequency around 0.8 GHz (mode 8) presents a null in the radiation pattern along the $+z$ axis its gain is low (Fig. 13), so it is highly preferred to either avoid its excitation or eliminate it by shifting it outside the working band. To get rid of the resonance frequency at 0.75 GHz since its gain is low, the shape of Ant2 is changed to a cross-shaped antenna (Ant3). This results in a high gain within the working band as clearly seen in Fig. 13; however, the band is still not improved which means that more modifications in the DRA are needed. Therefore, Ant4 is adopted which yields a good improvement in the matching as shown in Fig. 11. Additionally, it is seen that the two resonant frequencies are closer which is consistent with our characteristic mode analysis done in the previous section. It is important to note that such a cross-shaped structure is adopted to decrease the mutual interaction of the DRA elements in the array arrangement and decrease the weight of the whole antenna, especially when hundreds of antennas would be mounted on the base station tower for massive MIMO applications.

Finally, to improve the bandwidth and matching of the Ant4 to cover a wider frequency band, a notch is inserted into the second layer. As a result, the two fundamental modes TE_{111} (modes 2/3) and TE_{113} (modes 3/4) are shifted to 0.63 GHz and 0.8 GHz, respectively, and get much closer to each other, whereas the mode at 0.8 GHz is moved up to the high-frequency band and does not appear here as shown in Fig. 4. This has been verified by examining the magnetic field in the xz and yz planes and is not shown here for brevity. One can also observe a significant enhancement in the matching (from 1 dB to 7 dB at 0.75 GHz); therefore, the bandwidth is improved and reaches a value of 20.6%.

To show the effect of the notch on the bandwidth, a parametric study of the height of the notch g is given in Fig. 12. One can notice that as the gap increases the bandwidth improves. The best-optimized value is selected to be 14 mm.
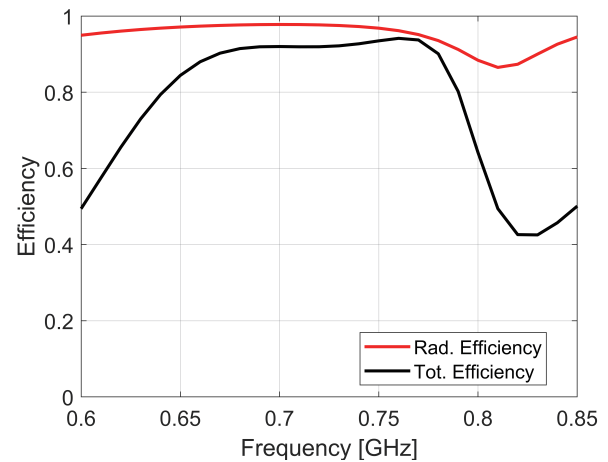
Finally, the total and radiation efficiencies of the proposed antenna over the frequency are shown in Fig. 14. The proposed design exhibits a high radiated efficiency of more than 85%, whereas the total efficiency decays a bit due to the non-perfect matching, but it is still more than 80% within the working band. We note that the drastic decay outside the operating band is due to the bad matching of the proposed antenna as shown in Fig. 11.

Table 3 summarizes the comparison between resonance frequency obtained by HFSS full-wave simulation (Fig. 11), CMA, and DWM theory. A good agreement among the three methods is achieved.

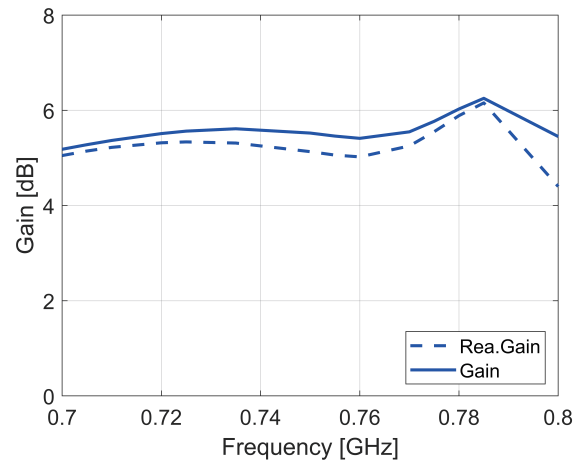## 3.2. Antenna Element Unit Cell in Massive MIMO System

For testing purposes, the proposed single DRA antenna has been included in a 3×4 array as shown in Fig. 15. The dimension of the single DRA ($0.2\lambda \times 0.2\lambda$) allows the development of the previous array with $1.29\lambda \times 1.5\lambda$ and an inter-element distance d_x and d_y along the x- and y-axes is 0.4λ which corresponds to the truncated subarray in Fig. 1. In this subarray, the antenna unit cell under test is the so-numbered 6th antenna which is surrounded by a dotted rectangle as shown in Fig. 15. Two metallic baffles are used to reduce mutual coupling between adjacent subarrays. The unit cell performances are examined for the nearest neighboring radiating element (namely the 2nd, 5th, 7th, and 10th elements). Moreover, the $+45°$ and $-45°$ polarizations of each element are denoted by T and B, respectively. The simulated S-parameters of the previous elements are presented in Fig. 16. The unit cell antenna in the massive MIMO scenario exhibits a wide bandwidth of 17.7% ranging from 0.67 to 0.8 GHz, whereas the coupling between the nearest neighboring unit cells is more than 13 dB in the whole band. The simulated gain and the realized gain of the unit cell antenna are examined and shown in Fig. 17. A stable gain of more than 5 dB is noticed over the operating band. The simulated radiation pattern of the unit cell antenna at 0.72 GHz is illustrated in Fig. 18.
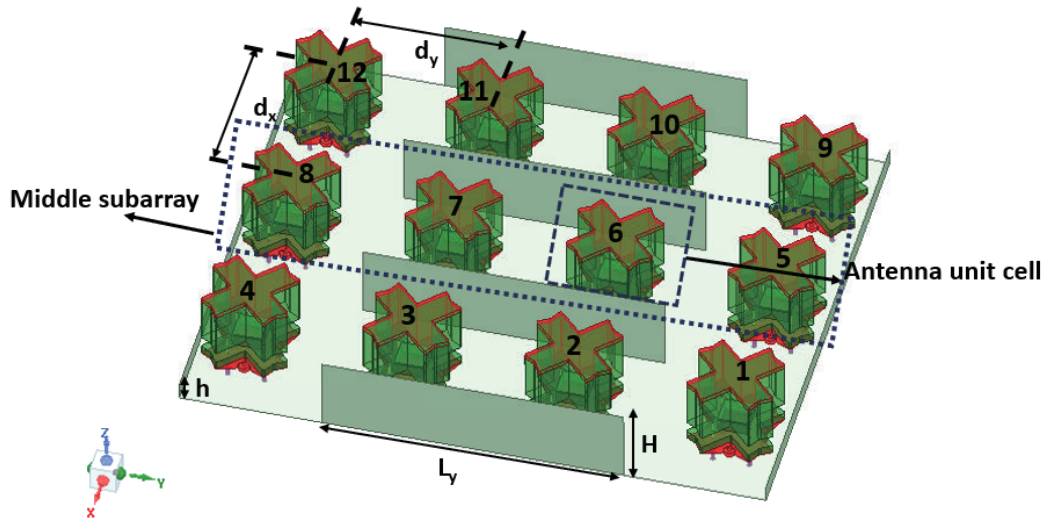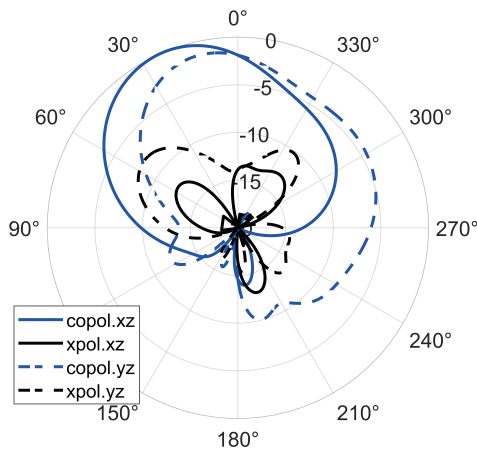
FIGURE 15. Proposed massive MIMO array with unit cell antenna in dashed lines and dimensions in mm: $d_x = d_y = 187$, $L_y = 250$, $H = 90$, $h = 20$.
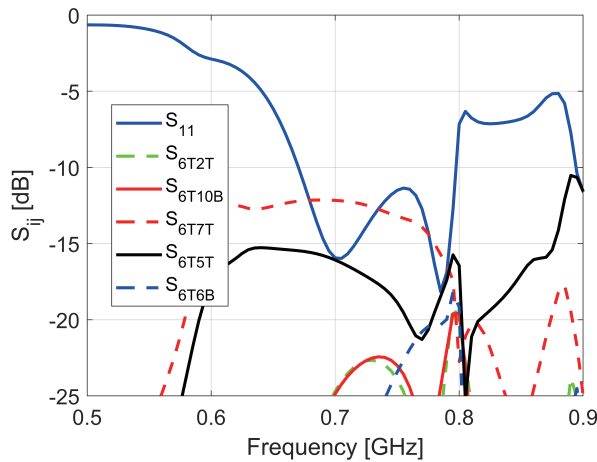
FIGURE 16. Simulated S-parameters of the unit cell antenna (element 6) in massive MIMO system.

FIGURE 17. Simulated gain of the unit cell antenna in massive MIMO system (element 6).

FIGURE 18. Simulated radiation pattern of the unit cell antenna in massive MIMO system at 0.72 GHz (element 6).

4. EXPERIMENTAL RESULTS AND DISCUSSIONS

A prototype is fabricated and measured to verify the DRA design's performance. The DRA element has been manufactured by injection molding and followed in the second step by computer numerical control (CNC) machining. Each block of the DRA is formed by gluing several thin plaques of 2.3 mm prepared from Preperm H2300HF and H1500HF materials with dielectric constants of 23 and 15 and loss tangents of 0.001 and 0.0037, respectively [34]. We note that other dielectric materials with similar dielectric properties are commercially available such as Magnesium Titanate ($\epsilon_r = 16$) and Lithium Ferrite ($\epsilon_r = 20$) from Hiltek Microwave Ltd [35, 36].

Figure 19 shows the assembly of the fabricated antenna. It is composed of three separated blocks that are stacked together with the help of plastic support (Fig. 19(b)).

Figures 20(a) and (b) show a comparison between the simulated and measured parameters of the 1×4 subarray config-
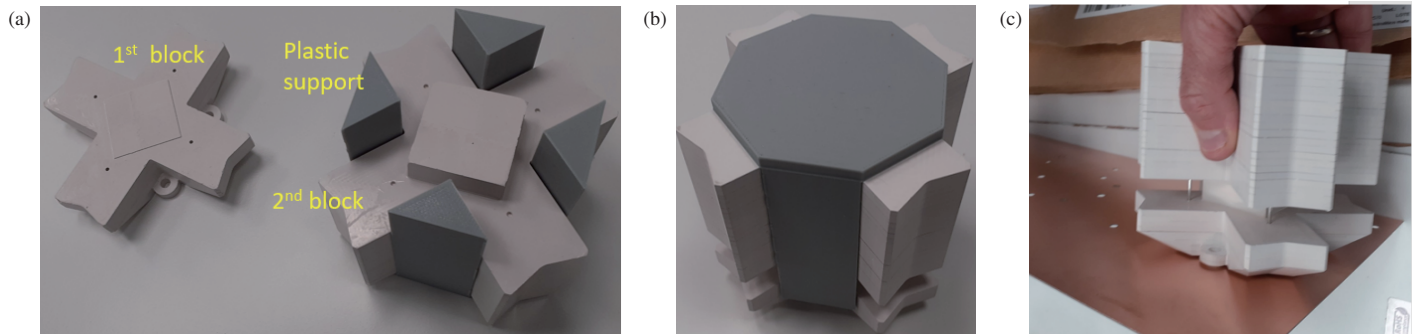
FIGURE 19. Proposed manufactured DRA (a) 1st and 2nd blocks (b) assembly with plastic support (c) side view of the whole assembly.
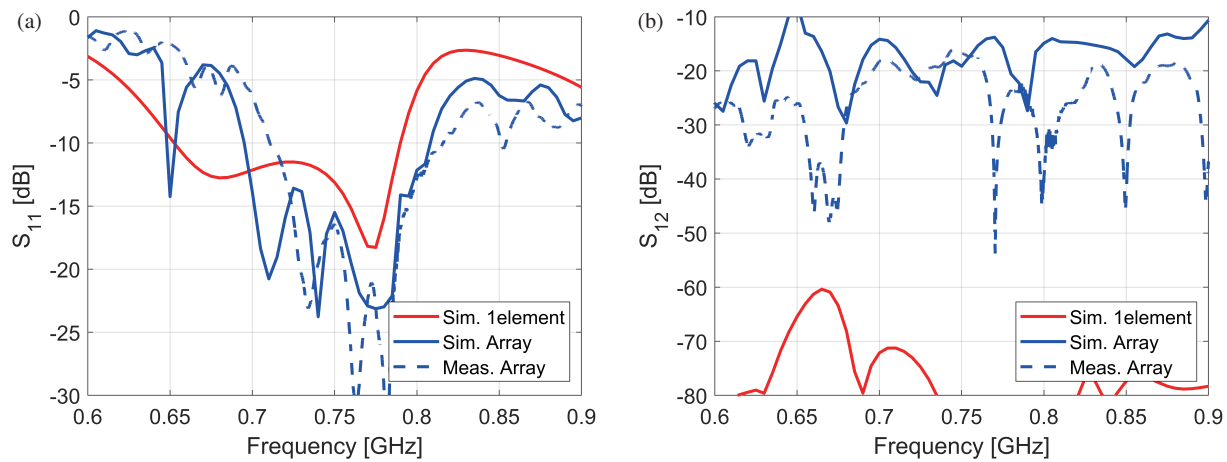

FIGURE 20. Different simulated and measured S parameters of 1 element and array (a) S_{11} (b) S_{12}.
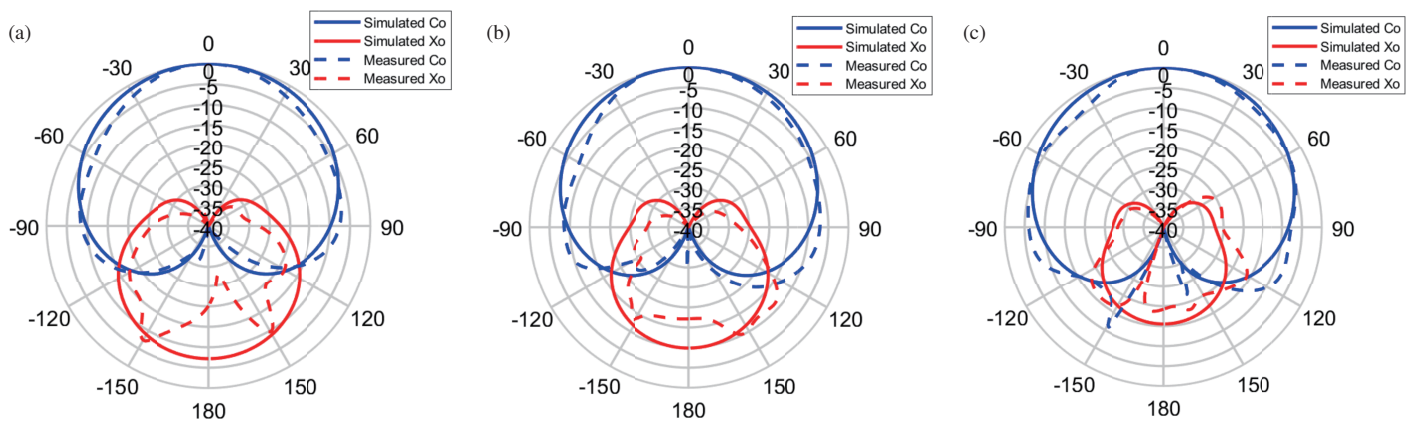

FIGURE 21. Simulated and measured radiation patterns of the proposed DRA (a) 700 MHz (b) 750 MHz (c) 800 MHz.

uration (Fig. 15) and the simulated isolated DRA element. A good agreement can be noticed for the S_{11} for either the array or the single DRA. The simulated bandwidth is 18.2% (0.65–0.78 GHz) for the single DRA, whereas the simulated and measured ones associated with the middle subarray in Fig. 15 are a bit narrower 13.15% ranging from 0.71 to 0.81 GHz which is due to the array effect (See Fig. 20(a)). Fig. 20(b) shows the simulated isolation between ports for the single DRA, which

is less than -60 dB within the operating band. This value is consistent with the differential feed that can suppress unwanted modes. When moving towards the array configuration, we can see that the isolation is decreased but with a good agreement between simulation and measurement for values lower than -17 dB over the working band.

Finally, Fig. 21 shows the proposed DRA's simulated and measured radiation patterns at different frequencies (700, 750,

TABLE 4. Comparison with recent works.

Ref. year	Bandwidth	Polarization	Size ($\lambda \times \lambda$)	Profile (λ)	Peak gain (dBi)	XPD (dBi)
[37] 2022	680–970 MHz (35%)	±45º	0.33 × 0.33	0.27	6.5	> 18
[38] 2020	4.79–5.03 GHz (4.88%)	±45º	0.5 × 0.5	0.05	8.45	> 20
[39] 2018	3.28–3.73 GHz (12.9%)	±45º	0.33 × 0.33	0.21	7	> 20
[40] 2022	4.4–5 GHz (12.8%)	H-V	0.47 × 0.74	0.11	5.4	> 20
[22] 2021	2.496–2.690 GHz (7.5%)	±45º	0.3 × 0.3	0.12	6	> 10
[41] 2022	25.93–30.25 GHz (15.5%)	±45º	0.34 × 0.36	0.1	6.8	> 15
[10] 2022	3.25–3.85 GHz (16.5%)	±45º	0.38 × 0.38	0.14	8.2	> 24
Our work	710–810 MHz(13.15%)	±45º	0.2 × 0.2	0.2	7	> 15

and 800 MHz). We note that since the design is symmetrical, horizontal and vertical planes are identical; therefore only one plane is shown here. One can observe stable radiation over the band with a good agreement between simulation and measured results. The cross-polarization level is more than 35 dB in the broadside direction in addition to a good front-to-back ratio.

Finally, Table 4 highlights the advantages of the proposed design compared with recent similar works. It is clearly seen that the proposed antenna presents the smallest size with a wideband and high gain. Although some works present a low profile such as [22, 37], their narrow band and large size limit their application in massive MIMO applications where the space is restricted.

5. CONCLUSION

This paper presents a new compact DRA ($0.2\lambda \times 0.2\lambda$) antenna with broadband and high gain radiation for MIMO array base station application. The miniaturization is achieved through a high permittivity technique which usually results in a narrow bandwidth. Therefore, CMA is used as a guiding tool to analyze a standard DRA, revealing that a pair of degenerate modes: M2/M3 and M4/M5 resonating at 0.4 GHz and 0.63 GHz can be used for dual-polarization performance providing that proper feeding is selected. Accordingly, reshaping the DRA in a cross-shaped along with an inserted gap showed that the two pairs are brought closer for broadband performance. As a result, a bandwidth of 21.6% is obtained with miniaturized size. Finally, the antenna element is examined in a massive MIMO configuration of 3×4, where good radiation performances are obtained.

REFERENCES

[1] Liu, Y., H. Yi, F.-W. Wang, and S.-X. Gong, "A novel miniaturized broadband dual-polarized dipole antenna for base station," *IEEE Antennas and Wireless Propagation Letters*, Vol. 12, 1335–1338, 2013.

[2] Martin-Anton, S. and D. Segovia-Vargas, "Fully planar dual-polarized broadband antenna for 3G, 4G and sub 6-GHz 5G base stations," *IEEE Access*, Vol. 8, 91 940–91 947, 2020.

[3] Yang, Q., S. Gao, Q. Luo, L. Wen, Y.-L. Ban, X.-X. Yang, X. Ren, and J. Wu, "Cavity-backed slot-coupled patch antenna array with dual slant polarization for millimeter-wave base station applications," *IEEE Transactions on Antennas and Propagation*, Vol. 69, No. 3, 1404–1413, 2021.

[4] Wen, L.-H., S. Gao, Q. Luo, Q. Yang, W. Hu, and Y. Yin, "A low-cost differentially driven dual-polarized patch antenna by using open-loop resonators," *IEEE Transactions on Antennas and Propagation*, Vol. 67, No. 4, 2745–2750, 2019.

[5] Huang, H., X. Li, and Y. Liu, "A low-profile, single-ended and dual-polarized patch antenna for 5G application," *IEEE Transactions on Antennas and Propagation*, Vol. 68, No. 5, 4048–4053, 2020.

[6] Lian, R., Z. Wang, Y. Yin, J. Wu, and X. Song, "Design of a low-profile dual-polarized stepped slot antenna array for base station," *IEEE Antennas and Wireless Propagation Letters*, Vol. 15, 362–365, 2015.

[7] Cui, Y., Y. Niu, Y. Qin, and R. Li, "A new high-isolation broadband flush-mountable dual-polarized antenna," *IEEE Transactions on Antennas and Propagation*, Vol. 66, No. 12, 7342–7347, 2018.

[8] Chen, Y. and C.-F. Wang, *Characteristic Modes: Theory and Applications in Antenna Engineering*, John Wiley & Sons, 2015.

[9] Tang, H., J.-X. Chen, W.-W. Yang, L.-H. Zhou, and W. Li, "Differential dual-band dual-polarized dielectric resonator antenna," *IEEE Transactions on Antennas and Propagation*, Vol. 65, No. 2, 855–860, 2017.

[10] Zhu, Y.-Y., J. Wang, J.-X. Chen, and W. Wu, "A compact wideband dual-polarized antenna using monolithic dielectric for 5G base station application," *IEEE Antennas and Wireless Propagation Letters*, Vol. 21, No. 9, 1717–1721, 2022.

[11] Zhao, S.-K., N.-W. Liu, Q. Chen, G. Fu, and X.-P. Chen, "A low-profile dielectric resonator antenna with compact-size and wide bandwidth by using metasurface," *IEEE Access*, Vol. 9, 29 819–29 826, 2021.

[12] Pan, Y. M., P. F. Hu, K. W. Leung, and X. Y. Zhang, "Compact single-/dual-polarized filtering dielectric resonator anten-

nas," *IEEE Transactions on Antennas and Propagation*, Vol. 66, No. 9, 4474–4484, 2018.

[13] Hu, P. F., Y. M. Pan, X. Y. Zhang, and S. Y. Zheng, "A compact filtering dielectric resonator antenna with wide bandwidth and high gain," *IEEE Transactions on Antennas and Propagation*, Vol. 64, No. 8, 3645–3651, 2016.

[14] Khan, S., H. Ali, M. Khalily, S. U. A. Shah, J. U. R. Kazim, H. Ali, and C. Tanougast, "Miniaturization of dielectric resonator antenna by using artificial magnetic conductor surface," *IEEE Access*, Vol. 8, 68 548–68 558, 2020.

[15] Lei, G. and L. K. Wa, "Dielectric resonator antenna," Patent, U.S. 10, 680,338 B2, Jun. 2020.

[16] Althuwayb, A. A., K. A. Abdalmalak, C. S. Lee, G. Santamaría-Botello, L. E. García-Castillo, D. Segovia-Vargas, and L. E. García-Muñoz, "3-D-printed dielectric resonator antenna arrays based on standing-wave feeding approach," *IEEE Antennas and Wireless Propagation Letters*, Vol. 18, No. 10, 2180–2183, 2019.

[17] Abdalmalak, K. A., A. A. Althuwayb, C. S. Lee, G. S. Botello, E. Falcón-Gómez, L. E. Garcia-Castillo, and L. E. García-Muñoz, "Standing-wave feeding for high-gain linear dielectric resonator antenna (DRA) array," *Sensors*, Vol. 22, No. 8, 3089, 2022.

[18] El Yousfi, A., A. Lamkaddem, K. A. Abdalmalak, and D. Segovia-Vargas, "A miniaturized triple-band and dual-polarized monopole antenna based on a csrr perturbed ground plane," *IEEE Access*, Vol. 9, 164 292–164 299, 2021.

[19] Komandla, M. V., G. Mishra, and S. K. Sharma, "Investigations on dual slant polarized cavity-backed massive MIMO antenna panel with beamforming," *IEEE Transactions on Antennas and Propagation*, Vol. 65, No. 12, 6794–6799, 2017.

[20] Gao, Y., R. Ma, Y. Wang, Q. Zhang, and C. Parini, "Stacked patch antenna with dual-polarization and low mutual coupling for massive MIMO," *IEEE Transactions on Antennas and Propagation*, Vol. 64, No. 10, 4544–4549, 2016.

[21] Yang, B., Z. Yu, Y. Dong, J. Zhou, and W. Hong, "Compact tapered slot antenna array for 5G millimeter-wave massive MIMO systems," *IEEE Transactions on Antennas and Propagation*, Vol. 65, No. 12, 6721–6727, 2017.

[22] Chen, Y., C. Zhang, Y. Lu, W.-W. Yang, and J. Huang, "Compact dual-polarized base station antenna array using laser direct structuring technique," *IEEE Antennas and Wireless Propagation Letters*, Vol. 20, No. 1, 78–82, 2021.

[23] Zhou, C., W. Yang, Q. Xue, Y. Liu, Y. Xu, and W. Che, "Millimeter-wave wideband dual-polarized LTCC antenna array based on metasurfaces for beam-scanning applications," *IEEE Transactions on Antennas and Propagation*, Vol. 70, No. 10, 9912–9917, 2022.

[24] El Yousfi, A., K. A. Abdalmalak, A. Lamkaddem, and D. S. Vargas, "Miniaturized broadband dual-polarized dielectric resonator antenna using characteristic modes," in *2023 17th European Conference on Antennas and Propagation (EuCAP)*, 1–4, Florence, Italy, 2023.

[25] Ye, L. H., G. R. Chen, X. Shi, R. Wu, J.-F. Li, and X. Y. Zhang, "Miniaturized broadband dual-polarized MIMO antenna array with stable radiation pattern for base station application," *IEEE Transactions on Antennas and Propagation*, Vol. 71, No. 8, 6688–6697, 2023.

[26] Petosa, A. and A. Ittipiboon, "Dielectric resonator antennas: A historical review and the current state of the art," *IEEE Antennas and Propagation Magazine*, Vol. 52, No. 5, 91–116, 2010.

[27] El Yousfi, A., A. Lamkaddem, K. A. Abdalmalak, and D. Segovia-Vargas, "A broadband circularly polarized single-

[layer metasurface antenna using characteristic-mode analysis," *IEEE Transactions on Antennas and Propagation*, Vol. 71, No. 4, 3114–3122, 2023.

[28] Petosa, A. and S. Thirakoune, "Rectangular dielectric resonator antennas with enhanced gain," *IEEE Transactions on Antennas and Propagation*, Vol. 59, No. 4, 1385–1389, 2011.

[29] Mongia, R. K. and A. Ittipiboon, "Theoretical and experimental investigations on rectangular dielectric resonator antennas," *IEEE Transactions on Antennas and Propagation*, Vol. 45, No. 9, 1348–1356, 1997.

[30] Alroughani, H. and D. A. McNamara, "The shape synthesis of dielectric resonator antennas," *IEEE Transactions on Antennas and Propagation*, Vol. 68, No. 8, 5766–5777, 2020.

[31] Leung, K. W., E. H. Lim, and X. S. Fang, "Dielectric resonator antennas: From the basic to the aesthetic," *Proceedings of the IEEE*, Vol. 100, No. 7, 2181–2193, 2012.

[32] Eisenstadt, W., R. Stengel, and B. Thompson, *Microwave Differential Circuit Design Using Mixed Mode S-parameters*, Artech, 2006.

[33] Petosa, A., N. Simons, R. Siushansian, A. Ittipiboon, and M. Cuhaci, "Design and analysis of multisegment dielectric resonator antennas," *IEEE Transactions on Antennas and Propagation*, Vol. 48, No. 5, 738–742, 2000.

[34] "Preperm," Available: https://www.avient.com/products/engineered-polymer-formulations/conductive-signal-radiation-shielding-formulations/preperm-low-loss-dielectric-thermoplastics.

[35] "Hiltek Microwave Ltd." Available: https://www.microwave-ferrite.com/.

[36] Luk, K. M. and K. W. Leung, *Dielectric Resonator Antennas*, Research Studies Press, 2003.

[37] Han, B., Q. Wu, C. Yu, H. Wang, X. Gao, and N. Ma, "Ultracompact dual-polarized cross-dipole antenna for a 5G base station array with a low wind load," *IEEE Transactions on Antennas and Propagation*, Vol. 70, No. 10, 9315–9325, 2022.

[38] Wang, X.-Y., S.-C. Tang, L.-L. Yang, and J.-X. Chen, "Differential-fed dual-polarized dielectric patch antenna with gain enhancement based on higher order modes," *IEEE Antennas and Wireless Propagation Letters*, Vol. 19, No. 3, 502–506, 2020.

[39] Zhang, Z.-Y. and K.-L. Wu, "A wideband dual-polarized dielectric magnetoelectric dipole antenna," *IEEE Transactions on Antennas and Propagation*, Vol. 66, No. 10, 5590–5595, 2018.

[40] Yang, G. and S. Zhang, "Dual-polarized wide-angle scanning phased array antenna for 5G communication systems," *IEEE Transactions on Antennas and Propagation*, Vol. 70, No. 9, 7427–7438, 2022.

[41] Cui, L.-X., X.-H. Ding, W.-W. Yang, L. Guo, L.-H. Zhou, and J.-X. Chen, "Communication compact dual-band hybrid dielectric resonator antenna for 5G millimeter-wave applications," *IEEE Transactions on Antennas and Propagation*, Vol. 71, No. 1, 1005–1010, 2023.

[42] Wu, R. and Q.-X. Chu, "A compact, dual-polarized multiband array for 2G/3G/4G base stations," *IEEE Transactions on Antennas and Propagation*, Vol. 67, No. 4, 2298–2304, 2019.

[43] Komandla, M. V., G. Mishra, and S. K. Sharma, "Investigations on dual slant polarized cavity-backed massive MIMO antenna panel with beamforming," *IEEE Transactions on Antennas and Propagation*, Vol. 65, No. 12, 6794–6799, 2017.](#)